



This is the accepted manuscript made available via CHORUS, the article has been published as:

Role of recombination kinetics and grain size in radiation-induced amorphization

Narasimhan Swaminathan, Dane Morgan, and Izabela Szlufarska

Phys. Rev. B **86**, 214110 — Published 27 December 2012

DOI: [10.1103/PhysRevB.86.214110](https://doi.org/10.1103/PhysRevB.86.214110)

The role of recombination kinetics and grain size in radiation induced amorphization

Narasimhan Swaminathan

*Department of Mechanical Engineering, Indian Institute of Technology Madras, Chennai, Tamil Nadu, India-600036**

Dane Morgan[†] and Izabela Szlufarska[‡]

*Department of Materials Science and Engineering, University of Wisconsin Madison,
1509 University Avenue, Madison, WI, USA-53706*

Using a rate theory model for a generic one-component material we investigated interactions between grain size and recombination kinetics of radiation-induced defects. Specifically, by varying parametrically non-dimensional kinetic barriers for defect diffusion and recombination, we determined the effect of these parameters on the shape of the dose to amorphization vs. temperature curves. We found that whether grain refinement to the nanometer regime improves or deteriorates radiation resistance of a material, depends on the barriers to defect migration and recombination, as well as on the temperature for the intended use of the material. We show that the effects of recombination barriers and of grain refinement can be coupled to each other to produce a phenomenon of interstitial starvation. In interstitial starvation a significant number of interstitials annihilate at the grain boundary leaving behind unrecombined vacancies, which in turn amorphize the material. The same rate theory model with material specific parameters was used to predict the grain size dependence of the critical amorphization temperature in SiC. Parameters for the SiC model were taken from *ab initio* calculations. We find that the fine grained SiC has a lower radiation resistance when compared to the polycrystalline SiC due to the presence of high energy barrier for recombination of carbon Frenkel pairs and due to the interstitial starvation phenomenon.

PACS numbers: 61.80.-x,61.82Rx,66.30.Pa,61.72Mm

Keywords: Nanocrystalline materials, recombination, radiation induced amorphization, silicon carbide, energy landscape

I. INTRODUCTION

One of the important concerns with ceramic materials considered for use as structural components in next generation nuclear reactors is the tendency of these materials to undergo radiation induced amorphization (RIA)¹. The eventual loss of long range order due to radiation results in a degradation of mechanical properties² as well as in an undesirable volume expansion³. One of the mechanisms that is believed to contribute to RIA is accumulation of radiation induced point defects, which in turn leads to an increase of the material's free energy to a level that is equal to the free energy of the amorphous state⁴. Interactions among the radiation-induced point defects, including interstitial-vacancy recombination, provide an intrinsic mechanism for annihilation of defects and for healing of the radiation damage. Even though very little can be done to alter or improve the intrinsic mechanisms, extrinsic engineering can facilitate annihilation of the defects by introducing sinks of point defects in the material. An efficient way to increase the density of sinks in the material is by reducing the grain size to the nanometer regime, thereby increasing the fraction of grain boundaries (GBs) which act as sinks for defects^{5,6}. Enhanced radiation resistance due to grain refinement has been observed in a number of metals, such as Pd⁷ and Au⁸, and non-metals, including Gd₂Ti_{0.65}Zr_{0.35}O₇⁵, MgGa₂O₄⁶ and TiN⁹. However, several works have also observed grain refinement resulting in an inferior resistance to radiation damage. For example, Refs.^{10,11} show that nanocrystalline (nc) ZrO₂ can be amorphized at a low dose of 0.9 dpa when compared to about 680 dpa required for the bulk material¹². Other material systems, such as Cu nanocrystals embedded in SiO₂ matrix¹³, also exhibited an inferior radiation resistance as compared to their coarse-grained counterpart.

The conflicting responses of fine grained materials to radiation motivates the need to better understand the interactions of radiation damage with microstructure, and in particular with GBs. Interactions of defects with GBs have been investigated extensively using classical molecular dynamics (MD) simulations performed on nanocrystalline or bi-crystal samples¹⁴⁻²⁷. While these studies provided significant insights into several aspects of cascade-GB interaction, the time scales simulated here mostly capture the primary damage, which occurs between a few tens of a picosecond to a nanosecond at the most, following the damage initiation. To extend the time scales accessible to MD and to understand the behavior of the radiation-induced defects over a time period of more than 300 nanoseconds, Bai *et. al.*^{20,27} employed a temperature accelerated dynamics (TAD). However, the phenomenon of RIA occurs over much longer time scales (from minutes to several years)²⁸ and these time scales are generally inaccessible to MD or TAD.

Experimental means of analyzing the resistance to RIA involves determining the dose to amorphization (DTA) vs temperature T curve for a given material²⁸. Useful insights into the kinetic processes that operate in the material are revealed when the DTA is determined for a range of temperatures^{1,29-31}. One particularly important feature of the DTA vs T curve is the critical temperature to amorphization (T_{cr})¹, which is the temperature beyond which no amorphization is possible at experimentally accessible dpa levels. Lower T_{cr} is evidence for more efficient intrinsic or extrinsic healing processes, which in turn correlates with a better radiation resistance of the material. Many insights into fundamental processes governing the kinetics of amorphization have been revealed using rate theory approaches, such as those developed for TiNi³² and Zr₃Fe^{33,34}. For example, it was found that in the case Zr₃Fe, both structural disorder (i.e., interstitials and vacancies) and chemical disorder (i.e., antisite defects) contribute significantly to RIA³⁴. The rate theory models mentioned above have certain simplifying assumptions in them such as treating the multi-component alloy as a single-component system³⁴ or considering that only defect complexes are responsible for amorphization and the individual point defects by themselves play no role. Despite the approximations, rate theory models reproduced a number of experimental features, such as the DTA vs temperature curves. Consequently, these models provide an excellent tool to investigating long-term radiation effects, and RIA in particular. To ensure the accuracy of the model, it is essential to correctly capture kinetic and thermodynamic properties of defects. In our earlier work³⁵, we determined such defect properties using *ab initio* calculations and we investigated the role of recombination energy landscapes on the radiation response of SiC. It was found that radiation resistance of SiC depends strongly not only on the migration barriers of defects, but also on the recombination barriers to various defect reactions.

The aforementioned rate theory models either neglect the role of GBs³³⁻³⁵ or homogenize the effects of GBs by introducing a grain size dependent sink term³². The approximations of homogenization of GB effects in the rate theory model results in requiring the modeling of temporal, but not spatial, evolution of the point defects. Furthermore, many of these studies were focused on micron sized grains and therefore the effects of grain size on the radiation resistance were not as pronounced as might be expected if the grain sizes are in the nanometer regime. A rate theory model for nc materials has been developed by Ovid'ko *et al.*³⁶. It was shown that nano-sized grains in the material can either lower or enhance resistance to RIA, depending on the grain size. While small grains provide a higher density of defect sinks and lead to healing of the damage, they also increase the free energy of the system due to the large contribution from the interfacial (GB) energy. A competition between these two contributions to the free energy of materials was proposed to be the reason for the seemingly contradicting experimental conclusions on the role of grain

size in radiation resistance (see earlier paragraphs). Although the model of Ovid'ko *et al.*³⁶ explicitly considered the spatio-temporal evolution of defects, the authors did not take into account the details of energy landscape for defect recombination and only one defect type was used in their model. Since we have recently shown that energy barriers to defect reactions can play an important role in radiation resistance³⁵, it is possible that the effects of recombination landscape and of grain size are coupled to each other. Here, we develop a rate theory model that includes both effects and allows investigation of their interplay. We first use this model to carry out a parametric study of a generic monoatomic material (or equivalently, a material where damage and defect evolution is effectively limited to one sublattice) to determine how various features of the DTA vs. T curve depend on the defect energy landscape and the grain size. We then apply the model to studies of silicon carbide, which is a promising material for structural applications in nuclear reactors³⁷. In the model for SiC, we capitalize on latest findings from state of the art *ab initio* calculations on details of defect energy landscapes in this material.

II. RATE THEORY MODEL

The rate theory framework for modeling radiation effects describes a spatio-temporal evolution of concentrations (c_n) of defects (n) produced during irradiation. n represents the type of the defect, namely vacancies, interstitials and antisites. The material is assumed to consist of spherical grains of radius R and the concentrations are assumed to be spherically symmetric, which means that they vary only along the radial direction. The differential equations that govern defect evolution as a function of time t and the corresponding initial and boundary conditions are

$$\frac{\partial c_n}{\partial t} = P_n + Q_n + \frac{D_n}{R^2} \frac{1}{r^2} \frac{\partial}{\partial r} \left(r^2 \frac{\partial c_n}{\partial r} \right), \quad (1)$$

$$c_n(t=0) = c_n^{eq}; c_n(t, r=1) = c_n^{eq}. \quad (2)$$

where c_n^{eq} is the thermal equilibrium concentration of defect n in the crystalline material, P_n is the rate of defect production and $Q_n(\frac{1}{\text{sec}})$ is the rate at which the concentration of defect n changes due to defect reactions. Both P_n and Q_n have units of ($\frac{1}{\text{sec}}$). Variable r corresponds to a non-dimensional radial distance defined as the ratio of the radial position to the total radius R , while D_n is the diffusion coefficient of species n , measured in the units of m^2/sec . The boundary conditions given in Eq. 2 represents a perfect sink situation.

Furthermore, in this paper we will also consider the case of an ‘‘ideal bulk’’ material with $R = \infty$. For the ideal bulk model there is no spatial variation in the concentrations of the defects because there are no external sinks of defects. Consequently, the differential equation (Eq. 1) becomes an initial-value problem and c_n , P_n and Q_n are functions of time only, representing an average value over a spatial domain. Correspondingly, equations Eq. 1 and 2 are reduced to

$$\frac{\partial c_n}{\partial t} = P_n + Q_n, \quad (3)$$

$$c_n(t=0) = c_n^{eq}. \quad (4)$$

The ideal bulk is a hypothetical case depicting a limiting scenario where no defect is allowed to annihilate at GBs or free surfaces of the material. Such situation, while strictly speaking is only possible in a single crystal of infinite size, can give significant insights into the kinetics of radiation-induced amorphization. For this reason throughout this study we will be comparing the calculated DTA vs. T curves for materials with finite grain sizes to such curves calculated for an ideal bulk.

A. Defect production (P_n)

Defect production in Eq. 1 is defined as $P_n = \Gamma \eta \alpha_n$ ³⁵. Here, Γ is the dose rate (dpa/s), η accounts for intracascade recombination and quantifies what fraction of displaced atoms survives as defects and α_n quantifies fraction of defect of type n . We consider two materials in this work: a one component-generic material X and SiC. In both cases we will use a high value of $\eta = 0.8$, as would be realized when material is irradiated with electrons²⁸. The value of Γ generally varies between 10^{-7} to 10^4 (See ref.²⁸) and depends on the material and other irradiation conditions. In this work, our goal is to determine the coupling between recombination landscapes and grain size on the radiation response and therefore the specific choice of Γ is not very important. Here, we chose Γ to be the same for the generic material X as for the SiC. This value is 2×10^{-3} dpa/s, which has been used in irradiation experiments of SiC^{29,38}. The value of α_n differs between the two materials simply by virtue of the number of components that make up the material. For the generic material (X), only two simple defects are possible, a vacancy V_X and an interstitial X_i . Since these

two defects are produced in equal quantities (as Frenkel pairs), α_n is 0.5 (see Table. I). For SiC, we consider six types of point defects that can be produced during irradiation of SiC on both sublattices of the material. These defects vacancies (V_C and V_{Si}), interstitials (C_i and Si_i), and antisites (Si_C and C_{Si}). Defect fractions α_n have been determined in MD simulations of displacement cascades induced with a 4 keV Si primary knock-on atom (PKA)²¹ and they are summarized in Table. II. We note here that the values of α_n for SiC were found to be independent of PKA energy and the grain size, as concluded in Ref.²¹.

B. Defect kinetics (Q_n and D_n)

Defect kinetics is controlled by both Q_n and the diffusion coefficient D_n (See Eq. 1). Q_n stands for the rate at which the concentration of defect n changes due to defect reactions and is a function of the concentrations of the species. For details, please see Ref.[35] and section 2.3 therein. In general, these defect reactions can lead to defect annihilation, formation of other simple point defects, or to formation of defect complexes. As elaborated in Ref.³⁵, different energy landscapes (no-barrier, recombination and trapping) are possible for the defect reactions. In the no-barrier landscape, only the migration of the defects govern the rate of a defect reactions. The recombination landscape involves a barrier for recombination which governs the rate of the reaction by virtue of that barrier being greater than the migration barrier of the fastest defect participating in the reaction. In case of the trapping landscape, a deep energy basin exists, which results in the formation of a complex. Furthermore, the reactions can be classified as being *diffusion dependent reactions* or *transformation reactions* (See Ref.³⁵ for details). In the case of the diffusion dependent type, the rate of the reaction depends on the ability of the defects to diffuse, and possibly overcome a barrier, before reacting with each other. Thus no-barrier and recombination reactions are typically diffusion reactions, while reactions involving overcoming a trap are not. The transformation reactions do not depend on the ability of the defects to diffuse, e.g, in reactions that overcome a trapped state to separate or recombine two defects.

For *diffusion dependent* reactions, which are of the type $A + B \rightarrow C$, the rate of the reaction is given by $K[A][B]$, where K is the rate constant and can be calculated from the following expression³⁹

$$K\Omega = 4\pi r_c(D_A + D_B) \times s \left(1 - \frac{s}{s+1}\right) \times (1 - \mathbf{erfc}((s+1)\sqrt{\tau})) \quad (5)$$

where

$$\mathbf{erfc}(x) = \frac{2}{\sqrt{\pi}} \exp(x^2) \int_x^\infty \exp(-t^2) dt \quad (6)$$

and $s = \exp(\bar{\beta}(E_m^q - E_b))$. E_m^q is the migration barrier of the fastest of the two defects participating in the reaction, E_b is the barrier for the reaction, $\bar{\beta} = (k_B T)^{-1}$, k_B is the Boltzmann constant, and T is the absolute temperature. In Eq. 5, Ω is the atomic volume, $\tau = t(D_A + D_B) \times (r_c)^{-2}$, where t is the time in seconds, r_c is the recombination radius for the reaction, D_n is the diffusion coefficient for defect n and is given by $D_0^n \exp(-\bar{\beta}E_m^n)$, where E_m^n is the migration barrier of defect n and D_0^n is a prefactor.

For *transformation reactions*, such as $C \rightarrow A + B$, the rates of the reaction are given by $R = \nu_0 \exp(-\bar{\beta}E_b) \times ([C])$. In the transformation reactions we will encounter in this article, C is a trapped defect complex, which dissociates into simple defects. The dissociation of the trapped complex into its constituent defects is modeled by replacing E_b with the trap barrier E_t . Note that in all the above expressions, the square brackets [] represent the concentration.

1. Defect kinetics for a generic material X

The purpose of considering a generic material is to perform a parametric study of how the DTA vs. temperature curve varies with grain sizes and with kinetic parameters, such as migration barrier for diffusion or the recombination barrier for a defect reaction. The only defect reaction we permit in this generic one-component material is Frenkel pair recombination, i.e., the annihilation of a vacancy and an interstitial ($V_X + X_i \rightarrow X_X$). This reaction is *diffusion dependent*, which means that its rate constant (Eq. 5) is a function of diffusion coefficients of V_X and X_i , the recombination barrier, and the recombination radius (r_c) (we assume no trapping). In our parametric study we vary the recombination barriers (E_b) and migration barriers (E_m) of defects. We represent the results in terms of non-dimensional parameters δ and ρ which are defined as $\delta = \frac{E_{V_X}}{E_{X_i}}$ and $\rho = \frac{E_b}{E_m}$. They correspond, respectively, to the migration energy of V_X and the recombination barrier E_b , normalized by the migration barrier of an interstitial X_i .

TABLE I. Parameters needed for the rate theory modeling of material X

Quantity (units)	Value	Notes
$E_m^{X_i}$ (eV)	0.67	Migration barrier of X_i ⁴³
$E_m^{V_X}$ (eV)	$\delta \times E_m^{X_i}$	Migration barrier of V_X (See section. II B 1)
E_b (eV)	$\rho \times E_m^{X_i}$	Barrier for recombination (See section. II B 1)
r_c (Å)	2.4	Recombination radius ⁴⁰ (See section. II B 1)
Ω (Å ³)	10.4	Atomic volume
$D_0^{X_i}$ (cm ² /s)	1.23×10^{-3}	^{35,42}
$D_0^{V_X}$ (cm ² /s)	7.26×10^{-4}	See section. II B 1
$\alpha_{X_i} = \alpha_{V_X}$	0.5	Fractions of defects in material X (See section. II A)
$E_f^{V_X}$ (eV)	4.193	Formation energy of V_X ⁴³
$E_f^{X_i}$ (eV)	6.953	Formation energy of X_i ⁴³
ΔE_{am} (eV/atom)	2.0	Amorphization energy ³⁵
γ (Jm ⁻²)	2.5	Grain boundary energy ⁴⁴

Changing δ thus alters D_{V_X} and governs relative ease with which the vacancy can annihilate at the GBs. Changing the value of ρ controls the rate of the recombination (K) of the Frenkel pairs in the material.

By varying ρ between 0.1 and 7, we change the energy landscape for defect reaction in material X from a no-barrier type to a recombination type³⁵. This approach allows us to consider landscapes in a wide variety of materials. For example, in metals no recombination barrier²⁸ is known to exist and therefore the lower limit for ρ is taken to be close to 0. Multi-component materials with directional bonding, such as SiC, have been recently discovered to have recombination barriers, which are substantially larger than the migration barriers of the defects participating in the reaction. Specifically, recent *ab initio* results suggest that the recombination barrier for the reaction of C_i with V_C could be as high as 1.35eV ($\rho > 2.0$) (⁴⁰). Parameter δ is varied between 1 and 7, which means that we always explicitly consider the migration barrier of the vacancy, to be at the least, equal to that of the interstitial migration barrier. Larger values of δ render the vacancy immobile when compared to the interstitials. For instance, in SiC where the V_C is less mobile when compared to C_i , $\delta \approx 6$. Low values of δ (e.g., $\delta < 1$) represent materials such as Si (⁴¹), for which $\delta \approx 0.5$, where the vacancy is more mobile than the interstitial. Although we do not explicitly discuss data for $\delta < 1$ such a domain is qualitatively equivalent to the ones we do discuss in this article. For values of $\delta < 1$ the interstitial and vacancy defects merely switch roles, in the sense that the barrier for interstitial migration is higher than the barrier for vacancy migration.

The grain radius along with the two non-dimensional parameters (ρ , δ) are used to study several features of the DTA vs T curve which are described in section III A below. These non-dimensional parameters are used to highlight how trends evolve in a manner as independent as possible of the specific interstitial migration barrier, as the qualitative trends in sign and relative magnitudes of various features of the DTA vs. T are governed by these relative values. It is to be noted that parameters ρ and δ together are not sufficient to yield a non-dimensional form of our systems governing differential equations 2. In other words, the family of simulations that correspond to a given value of ρ and δ will not all yield the same DTA curves. Specific choices for the interstitial migration barrier, diffusion coefficient, recombination radius, and defect and amorphization energies, could all change temperatures and doses at which the different features of the DTA vs T curve occur, even for a given set of ρ and δ . However, the changes in the features of the DTA vs T curve between a nano crystalline sample and a bulk sample will be qualitatively similar for similar values of ρ and δ . In the case of a generic material, our choice of many of the parameters is guided by values relevant for SiC³⁵. Specifically, the value of $E_m^{X_i}$ is taken to be the migration barrier of C_i (See Table. III), while r_c is taken to be that belonging to the recombination reaction ($C_i + V_C \rightarrow C_C$). The D_0^n values for the vacancy (V_X) and the interstitial X_i are taken to be that of V_C and C_i ^{35,42}, respectively. All the values for material X are tabulated in Table. I for easy reference.

2. Defect kinetics for SiC

For the case of SiC, we consider six defect reactions which are summarized in Table III. The recombination radius (r_c) and the required barriers for all the reactions are also provided in this table. Reactions R.2, R.3 and R.4 have the same barriers as in Ref.⁴⁰. Reactions R.5 and R.6 were not considered in Ref.⁴⁰. Energetics of these reactions was recently reported by Zhang *et. al.*⁴⁵. It was found that R.5, which involves the Si_i kicking out a C_{Si} , has the no-barrier landscape while R.6 (C_i kicking out a Si_C) has the trapping energy landscape. Reaction R.6 involves two

TABLE II. Fraction α_n , Migration (E_m^n) and formation (E_f^n) energies of defect n considered for SiC.

Defect(n)	α_n ³⁵	E_f^n (eV)	E_m^n (eV)
V _C	0.330	4.193 ⁴³	3.661 ⁴³
C _i	0.380	6.953 ⁴³	0.670 ⁴³
V _{Si}	0.084	4.966 ⁴³	2.400 ⁴³
Si _i	0.035	8.754 ⁴³	0.829 ⁴³
C _{Si}	0.063	4.034 ⁴³	2.400 ⁴³
Si _C	0.110	3.564 ⁴³	3.661 ⁴³
C _i -Si _C	0	9.317 ⁴⁵	∞

TABLE III. Defect reactions for the SiC rate theory model

Reaction #	Defect Reaction	E_b (eV)	r_c (Å)
R. 1	V _C + C _i → C _C	0.92 ⁴⁵	2.1 ⁴⁰
R. 2	V _{Si} + Si _i → Si _{Si}	0.03 ⁴⁰	6.3 ⁴⁰
R. 3	V _C + Si _i → Si _C	1.11 ⁴⁰	3.7 ⁴⁰
R. 4	V _{Si} + C _i → C _{Si}	1.25 ⁴⁰	3.3 ⁴⁰
R. 5	Si _i + C _{Si} → Si _{Si} + C _i	0.66 ⁴⁵	6.3 (Assumed to be the same as R. 2)
R. 6 ₁	C _i + Si _C ↔ C _i -Si _C	0.69 ⁴⁵	2.1 (Assumed to be the same as R. 1)
R. 6 ₂	C _i -Si _C → C _C + Si _i	1.35 ⁴⁵	Not applicable

half reactions, R.6₁ and R.6₂. R.6₁ involves formation of the complex C_i-Si_C from isolated C_i and Si_C. Reaction R.6₂ involves a kick out, where the complex dissociates to form Si_i and C_C. R.6 is comprised of both *transformation* reactions (backward reaction of R.6₁ and forward of R.6₂) as well as *diffusion dependent* reactions (forward reaction of R.6₁). We note that there has been conflicting reports of the energy landscape for R.1 (recombination of V_C with C_i)^{40,46,47} and we use the most recent analysis given in Ref.⁴⁵.

The diffusion coefficients D_n for each defect n is needed to model the explicit diffusion of the defects as well as to quantify the reaction rate in diffusion dependent reactions (Eq. 5). For interstitials and vacancies $D_n = D_0^n \exp(-\beta E_m^n)$ where the prefactor D_0^n is 1.23×10^{-3} cm²/s and 3.30×10^{-3} cm²/s for the C_i and Si_i, respectively⁴². For vacancy diffusion in an fcc crystal, D_0^n can be estimated as $0.7815\nu_0 \frac{a_0^2}{2}$, where $\nu_0 = 10^{12}$ Hz and $a_0 = 4.31$ Å is the lattice constant for β -SiC. To determine D_n for carbon (silicon) antisites we treat these defects as impurities on the silicon (carbon) sublattice. We then use a simplified “two frequency” model as done in Ref.³⁵ to calculate the diffusion coefficients of the antisites. The final expressions for the two antisites are

$$D_{C_{Si}} = \frac{a_0^2}{2} \nu_0 \exp(-\bar{\beta} E_m^{V_{Si}}) f[V_{Si}] \quad (7)$$

$$D_{Si_C} = \frac{a_0^2}{2} \nu_0 \exp(-\bar{\beta} E_m^{V_C}) f[V_C] \quad (8)$$

where

$$f = \frac{2 + 7F}{2 + 7F + 2\epsilon}. \quad (9)$$

f is the correlation factor, ϵ needed for calculating f depends on the defect type and is equal to $\epsilon_{C_{Si}} = \exp(-\bar{\beta} E_m^{V_C}) / \exp(-\bar{\beta} E_m^{V_{Si}})$ for C_{Si} is and to $\epsilon_{Si_C} = \exp(-\bar{\beta} E_m^{V_{Si}}) / \exp(-\bar{\beta} E_m^{V_C})$ for Si_C. F is a fairly complicated function of the ratio of the jump frequencies of the vacancies. The details of the expression for F can be found in⁴⁸⁻⁵⁰. Based on the above approximations we calculated F to be being equal to 0.736³⁵.

C. Amorphization criterion

In our study, the material is considered amorphized when the cumulative energy of all point defects, defect complexes, and the energy contributed by the GBs becomes equal to the energy difference (ΔE_{am}) between the amorphous and the crystalline phases. Such a criterion is known to be applicable to many semiconductor materials⁴ and therefore seems a reasonable approach to model SiC.

To predict amorphization in the generic material X or in SiC, we need to know a number of thermodynamic parameters that include formation energies of each defect, GB energy (γ), and ΔE_{am} . For simplicity, we assume that the defects in material X have the same formation energies as the defects on the C sublattice of n -type SiC. The GB energy for the generic material X is taken to be $\sim 2.5 \text{ Jm}^{-2}$, which is comparable to GB energies in SiC⁴⁴. ΔE_{am} is taken to be 2.0 (eV/atom), which is also comparable to the value of 1.93 eV/atom used for SiC in earlier *ab initio* based rate theory models³⁵. All the necessary thermodynamic parameters for material X and for SiC are summarized in Table. I and Table. II, respectively.

For the ideal bulk, the amorphization criterion takes a simple form

$$\sum_{i=1}^N E_f^i c_i(t_{am}) = \Delta E_{am} \quad (10)$$

where N is the total number of defects, c_i is the concentration of defect i and t_{am} is the time when the above equation is satisfied. Based on the time to amorphization t_{am} predicted by Eq. 10, one can calculate the dose to amorphization as the dose rate $\times t_{am}$. By calculating such dose to amorphization at different temperatures, we can determine the DTA vs temperature curve for the material.

A mathematical criterion for amorphization in materials with finite grain sizes is somewhat more complex. One reason is that even though we considered uniform radiation damage, we found in simulations that the relative differences in the diffusion kinetics of the different defects can cause the material to amorphize heterogeneously. Specifically, at low temperatures when no recombination is possible, defects near the GBs can diffuse and annihilate there. This phenomenon causes amorphization to proceed from the center of the grain towards the GB. In the case of very high temperatures, recombination is active in the center of the grain and defects annihilate. However, near a GB the most mobile defects annihilate, leaving behind an excess of the less mobile defects, which in turn leads to a local amorphization of the material. This unbalanced annihilation of defects near the GBs results in the amorphization proceeding from the GB towards the center of the grain. Consequently, when deciding on the criterion for amorphization in materials with finite grain size, we considered two different methods for obtaining DTA vs. T curves. These methods are discussed below.

1. Method 1 (Average concentration method)

Following the scheme from Ovidko³⁶, we use a volume-averaged concentration of defects in the entire grain at a particular temperature and we predict amorphization using the following expression.

$$\sum_{i=1}^N E_f^i \bar{C}_i(t_{am}) + \gamma \frac{3\Omega}{R} = \Delta E_{am} \quad (11)$$

where N is the number of defects in the material, E_f^i is the formation energy of defect i , $\bar{C}_i = \frac{1}{V} \int c_i dv$ is a volume averaged concentration c_i of defect i , and t_{am} is the time at which Eq. 11 is satisfied. Once t_{am} is known, the DTA can be calculated as $t_{am} \times \text{dose rate}$ (dpa/s). The problem with this method as applied to our system is that at higher temperatures unrealistic concentrations of immobile defects can be produced, especially near the boundary of the domains. Such unphysical concentrations can be overcome by using a moving boundary method, where amorphization is modeled as a heterogeneous phenomenon and is described below.

2. Method 2 (Moving boundary method)

In this method, we first divide the domain into many bins, with the bin width being equal to the thickness of a monoatomic layer ($\sim 1\text{\AA}$). Then the material inside of a bin is considered to have been amorphized at time \bar{t} , if the following condition is satisfied,

$$\sum_{i=1}^N E_f^i c_i(\bar{t}) + \gamma \frac{3\Omega}{R} = \Delta E_{am}. \quad (12)$$

If the amorphization proceeds from the GB toward the center it can be modeled by simply decreasing the grain radius by one monoatomic layer as soon as the material in the outermost bin amorphizes. Defect evolution can then continue until the condition given by Eq. 12 is met again in the bin that neighbors the GB. This process is carried

on until at time t_{am} a significant fraction (here, we chose 90%) of the grain interior has been amorphized. During this heterogeneous amorphization, all the GBs are increasing in width until the entire material has amorphized. The GBs are treated as perfect sinks of defects throughout the entire simulation. We found that the inclusion of this heterogeneity in the rate theory model did not affect the qualitative aspects of the DTA vs. T curves of the finite grain size material when compared to that of the ideal bulk (see section.IIC3).

When the process of amorphization proceeds from the center towards the GB, an uncertainty arises regarding the treatment of the newly formed amorphous material at the center of the grain. If this amorphous region is treated as a perfect sink (similarly to the GB), then the bin that amorphizes at a subsequent time is located somewhere between the first bin (located near the center) that amorphized and the GB. This phenomenon occurs because the defects can now diffuse and annihilate at both the boundaries (inner amorphous region and the GB). Such heterogeneous distribution of amorphous regions creates a heterogeneous distribution of sinks and cannot be easily tracked in our model. On the other hand, it seems unrealistic to treat the inner amorphous material as an imperfect sink. It is unclear how one should handle this inner domain of amorphous material and we therefore made an approximation. Furthermore, since the heterogeneity involving the amorphization of finite-grain sample from the GB towards the center did not affect the qualitative results significantly (see previous paragraph and section IIC3), we ignore potential effects of the formation of the inner amorphous region. Specifically, we do not treat the inner amorphous region as a sink and once we find that the material began amorphizing from the center, we irradiate the material until t_{am} , which is a time corresponding to 90% of the material being amorphized.

3. Comparison of the average concentration method and the moving boundary method

Although the moving boundary method appears more realistic because it captures the correct physics of defect evolution, this method is computationally expensive because amorphization has to take place one monoatomic layer at a time. Here we compare the DTA vs. T curves produced by the two methods for material X , to determine if the moving boundary conditions are necessary. In Fig. 1 we show DTA vs. T curves for selected values of kinetic parameters ($\delta = 1, 2$ and $\rho = 0.1, 1$ and 2). Data is shown for grain radius $R = 10$ nm (dashed lines) and for an ideal bulk (solid lines). The observed trends in the DTA vs T are qualitatively similar between the two methods. For $\delta = 1$, the curves for the 10 nm case either coincide with the curve of the ideal bulk (for values of $\rho = 0.1$ and 1) or are shifted to the left with respect to the bulk curves (for $\rho = 2$). These trends are quite similar for both methods of modeling the amorphization. The temperature at which the DTA value begins to increase for the 10 nm case are also similar between the two methods for all ρ values. For $\delta = 2$ case, all values of ρ produce a step for the 10 nm material. Even though the steps occur at slightly different doses and the width of the steps are slightly different for the two methods, when the features are compared to those of an ideal bulk material it is clear that the two methods produce the same qualitative behavior. Because of these similarities, in this study we will use the average concentration method, which choice leads to significant savings in the computational time.

III. RESULTS AND DISCUSSION

A. DTA vs temperature curves

First, we examine the DTA vs T curves for the material X in order to identify and define certain key features of the curve, which will be studied parametrically later. Figure 2 compares DTA vs. T curves obtained for the 10 nm grain size (dashed red lines) to those determined for the ideal bulk (thick black lines). The curves are plotted for $\delta = 5$ and for a number of different values of ρ , where the numbers on the lines correspond to ρ values. There are a number of observations that can be made based on this plot. For the ideal bulk and low values of ρ ($\rho = 0.1, 0.5$, and 1), the curves coincide. A characteristic feature of these curves is a dramatic increase at a certain temperature (here it is ~ 200 K), which is referred to as the critical amorphization temperature T_{cr} . Beyond T_{cr} it is very difficult to amorphize the material. Increasing the value of ρ above unity increases T_{cr} . $\rho > 1$ means that barrier to recombination of Frenkel pairs is larger than the migration barriers of interstitials in the material. The reason for the observed trend of T_{cr} with ρ is that higher ρ values require higher temperatures to initiate the recombination reaction and recombination is the only means by which the material can heal radiation-induced damage.

The curves for the 10 nm grains show a richer set of features, and more specifically they exhibit steps of constant DTA. Such steps in the DTA vs T curves have been seen for Zr_3Fe irradiated with Ar ion³³ and possibly for electron irradiated SiC^{38,51}. To understand the physical phenomena controlling the shape of the DTA vs. T curve, we first define the different features in the curve using the case of $\rho = 2$ (Fig. 2) as an example. The curve shows first an

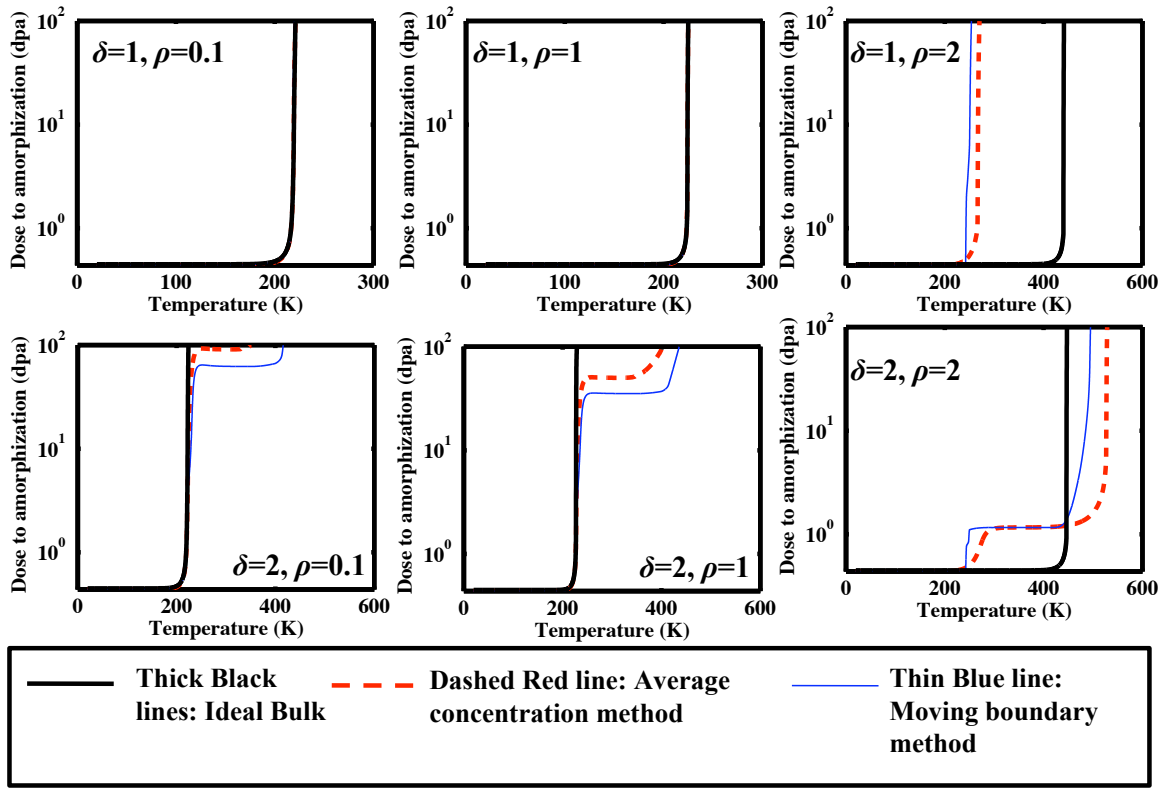


FIG. 1. Comparison of the DTA vs T plot for the ideal bulk (black thick line) and material with grain size of 10 nm (dashed line). The plots are made for the generic material X . Red dashed and thin-blue lines correspond to the average concentration method and moving boundary method, respectively. For values of $\delta = 1$, $\rho = 0.1, 1$ the DTA vs. Temperature curves for the nanomaterial (using either of the two methods) and the ideal bulk coincide and are hence indistinguishable.

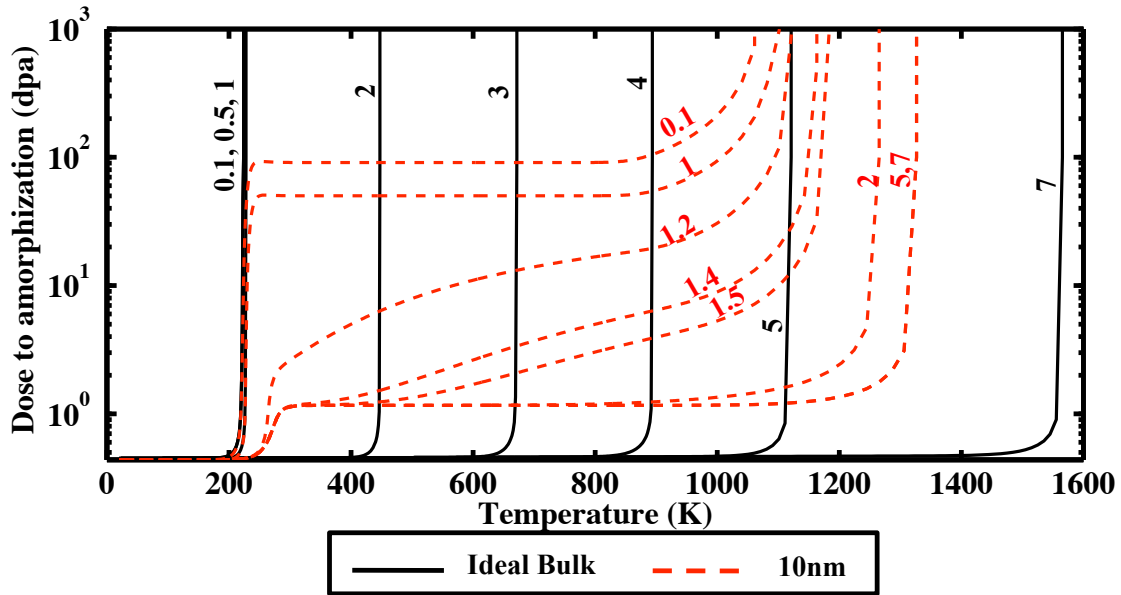


FIG. 2. The DTA vs T plot for $\delta = 5$. Numbers on the lines indicate the values of ρ . The thick black lines correspond to the ideal bulk case, while the red dashed lines represent materials with a 10 nm grain diameter. The DTA vs. T curve, for the 10 nm case, for values of $\rho = 5$ and 7 coincide and are hence indistinguishable.

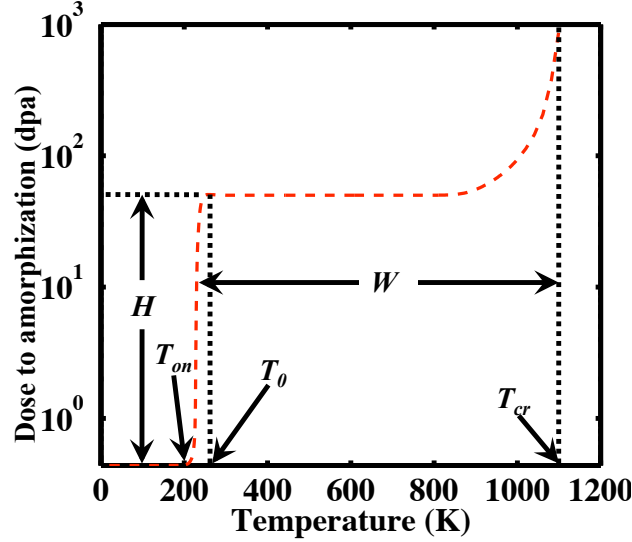


FIG. 3. A plot showing the various features (T_{on} , W , T_{cr} and H) of the DTA vs. T plot.

increase in DTA at around ~ 250 K and then reaches a plateau at a dose of ~ 1 dpa. The plateau extends until the temperatures of ~ 1500 K, above which the curve once again begins to increase rapidly, defining the T_{cr} . The temperature of initial increase (~ 250 K for $\rho = 2$) will be referred to as the *onset temperature*, T_{on} . The dose at which a plateau occurs will be referred to as the *step height*, H , while the difference between the T_{cr} and T_{on} will be called the *step width*, W . It is interesting to point out that H is larger for $\rho \leq 1$ than it is for $\rho > 1$. In addition, while the plateaus are sharp for $\rho \leq 1$ and for $\rho > 2$, the plateaus for curves with intermediate values of ρ are less pronounced. In the latter case, there is however still a clear distinction between T_{on} and T_{cr} . Furthermore, we note that for $\rho \leq 5$, T_{cr} for the 10 nm grain size is higher than T_{cr} of an ideal bulk, while for values of $\rho > 5$ we observe the opposite trend. This behavior suggests that materials having critical combinations of kinetic parameters and grain size, the nanomaterial can be more susceptible to radiation damage than the coarse grained material. Finally, we note that for the ideal bulk material, T_{on} and T_{cr} coincide, irrespectively of the value of ρ .

In subsequent sections we investigate the dependence of the different features of DTA vs. T curves (which are T_{on} , W , T_{cr} and H , see Fig. 3) on ρ , δ , and the grain radius R . The features of the curves are identified as follows. We first calculate the derivative of the dose to amorphization with respect to the temperature and we plot this derivative against temperature. For a typical DTA vs T curve with a step, this derivative plot will exhibit two maxima. The onset temperature T_{on} corresponds to the first maximum while T_{cr} coincides with the second maximum. To determine H , we need to calculate the dose that corresponds to the plateau. This dose H is calculated using interpolation. We interpolate the value of H from the DTA vs T data for a temperature that is the average of T_{cr} and T_{on} .

B. Generic material X, Variation of (T_{on} , W , T_{cr} and H)

In Figs. 4a-d, we plot the variations in T_{on} , W , T_{cr} and H with respect to ρ , for three values of R and three values of δ . In Figs. 5a-d, variation in the same properties is plotted with respect to R , for two values of ρ (0.1 and 2) and three values of δ .

1. Onset temperature, T_{on}

The onset temperature T_{on} (Fig. 4a) is independent of the value of δ and increases with ρ in the range $0 < \rho < 2$. The increase ranges from about 50K for the 10 nm and 25 nm grains to about 175K for the 1 μm grain. This increase is quite small when compared to the corresponding changes in T_{cr} or W , as can be seen in Figs. 4b and c. As ρ increases above 2, the value of T_{on} remains constant. Furthermore, increasing grain size (at a constant value of ρ) leads to an increase in T_{on} (Fig. 5a). To understand the trends in T_{on} , one needs to first realize that the onset temperature is

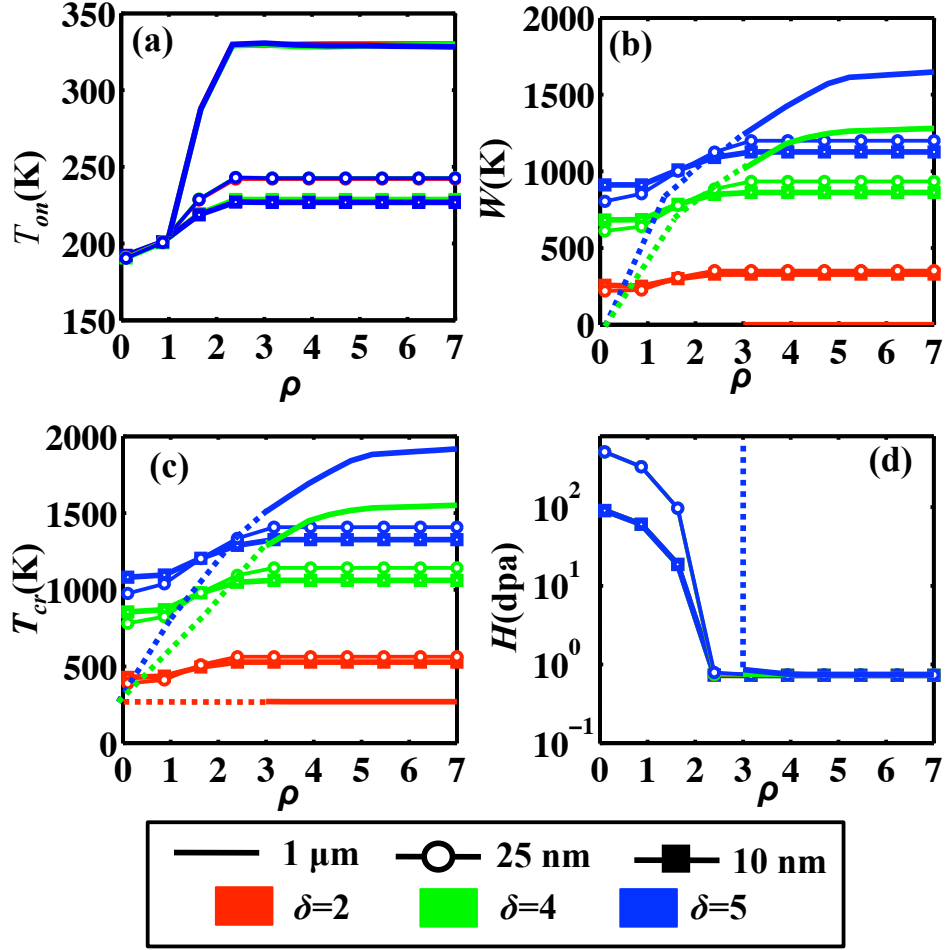


FIG. 4. (a) Onset temperature (T_{on}) (b) Width (W) (c) Critical amorphization temperature T_{cr} and (d) Step height (H), as a function of ρ . Bare lines represent $R = 1 \mu\text{m}$, lines with squares - $R = 10 \text{ nm}$ and lines with circles - $R = 25 \text{ nm}$. The red, green, and blue colors correspond to $\delta = 2, 4$ and 5 , respectively. For $1 \mu\text{m}$ grain size, the dotted lines in the W , T_{cr} and H plots show possible trends inferred based on the behavior of these quantities (W , T_{cr} and H) with increasing grain sizes (See text in section. III B 2)

controlled by a combination of two factors, defect recombination and defect annihilation at GBs. Since ρ corresponds to a normalized energy barrier to defect recombination, increasing ρ suppresses recombination of Frenkel pairs and annihilation of defects at GBs becomes the dominant effect in healing of radiation damage. For T near T_{on} , the defects migrating and annihilating at GBs are interstitials. Recombination of Frenkel pairs is almost entirely suppressed for $\rho > 2$ and because the process of annihilation of defects at GBs does not depend on ρ in this regime, neither does T_{on} . T_{on} , however, increases with the grain size because the larger the grain, the longer the distance that interstitials have to travel to annihilate at GBs (Fig. 5a corresponding to $\rho = 2$).

In contrast, at very low values of ρ , only interstitials residing near GBs can be annihilated there and the majority of defects are removed by Frenkel pair recombination and hence the value of T_{on} is independent of R as can be seen in Fig. 5a corresponding to $\rho = 0.1$. For intermediate values of ρ (between 0 and 2), some of the interstitials can recombine with vacancies and some of the interstitials migrate to GBs. As a result, unrecombined defects located at the grain interior will have to traverse greater lengths to annihilate. The larger the recombination barrier (ρ), the larger the fraction of defects that will need to travel to GBs to anneal. Consequently, the effective length that interstitials need to diffuse to be annihilated is also larger, resulting in an increase of T_{on} with increasing ρ .

2. Width W and Critical temperature for amorphization T_{cr}

In Fig. 4b we plot W as a function of ρ , where W is the width of the step in the DTA vs T curve. For the 10 nm and 25 nm cases, we found the steps in the DTA vs. temperature curves to occur at doses < 1000 dpa while that for the 1 μm case the steps occurred at doses > 1000 dpa. Therefore, for the nanosized grains, the behavior of W for the entire range of ρ was captured, while that for the 1 μm the behavior was captured only for $\rho > \approx 3$. In order to complete the curves for the 1 μm case for $\rho < 3$, we first plot the variation of W with grain size for different values of ρ and then we extrapolate W to the grain size of 1 μm . The variations of W with R for two values of ρ (0.1 and 2) and for three δ values are shown in Fig. 5b. We found that steps in the DTA vs. T occur below 1000 dpa only for $R < \approx 30$ nm. However, even in this regime of grain sizes, there is a clear decreasing trend of W with R for $\rho = 0.1$ while for $\rho = 2$, W is only weakly dependent on R . By extrapolating the trends in Fig. 5b we find that for $\rho = 0.1$, W is equal to zero (there is no step in the DTA vs T curve) beyond a certain value of R . This value of R depends on δ , and it is $\sim 10, 25$ and 50 nm, respectively, for $\delta = 2, 4$, and 5 . We are now ready to extrapolate the W vs ρ curve in Fig. 4b for the grain size of 1 μm . For this grain size, $W = 0$ at $\rho = 0.1$ for all the δ values considered. At $\rho = 2$, the value of W is independent of the grain size and for $\rho > 3$ we have data available for W directly from simulations (solid lines). Using the three values of W at $\rho = 0.1, 2$, and 3 , we interpolated the data for the entire range of ρ as shown by dotted lines in Fig. 4b.

We note that W is equal to the difference between T_{cr} and T_{on} . Consequently, once the variations of W with ρ and R are known, the corresponding variations in T_{cr} can be found out by adding T_{on} and W (see Figs. 4c and 5c). We saw in Section IIIB1 that the increase in T_{on} over the entire range of ρ is small compared to the increases in T_{cr} , therefore changes in W are a reflection of changes in T_{cr} (since $T_{cr} = T_{on} + W$) and the variations of both W and T_{cr} are governed by the same physics. The critical temperature T_{cr} for a one component material with nanosized grains is set by vacancy migration barrier, similarly to how T_{on} was set by interstitial annihilation (see section IIIB1). For a given δ , change in T_{cr} with ρ is qualitatively very similar to the change in T_{on} with ρ . Trends in T_{cr} with ρ can be explained by considering vacancy motion and applying similar arguments as we have made earlier to explain T_{on} using interstitial motion.

Interesting features in the functions of W and T_{cr} vs ρ occur at low values of ρ (Figs. 4b,c and 5b,c, respectively). In particular, for $\rho < \approx 2$, T_{cr} decreases with an increasing grain size, which means that materials with a lower grain size have an inferior resistance to RIA when compared to their coarse grained counterparts. The reasons underlying this behavior will be discussed in detail in the next section.

3. Variation of T_{cr} with R for $\rho < 2$

In order to understand the decrease in T_{cr} with increase in R for $\rho < 2$ (see Fig. 4c) we compare the behaviors of two extreme grain sizes and analyze their defect kinetics in detail. In particular we will study the behaviors of the ideal bulk and the 10 nm cases for two values of ρ (0.1 and 2), while keeping $\delta = 5$. We begin by discussing features in the DTA vs. T curve shown in Fig. 2 for the ideal bulk and 10 nm cases. We note that for $\rho = 0.1$, T_{on} for both curves coincide. For $\rho = 2$ T_{on} for the 10 nm case is ~ 250 K, while for the ideal bulk case it is ~ 450 K. To understand which mechanism (recombination or annihilation at GB) is responsible for T_{on} , in Fig. 6a we plot the rates of the recombination reactions for the two grain sizes and the two values of ρ . We find that for $\rho = 0.1$, for both the bulk and the 10 nm cases, the rate of the reaction becomes greater than zero and increases rapidly at ~ 250 K, coinciding with T_{on} . This observation suggests that for $\rho = 0.1$, Frenkel pair recombination contributes most to the healing process. For $\rho = 2$, we find that the reaction rate for the bulk begins to increase at ~ 450 K, coinciding with $T_{cr} = T_{on}$, which suggests that recombination of Frenkel pairs is the active healing mechanism. However, for $\rho = 2$ and grain size of 10 nm, the reaction rate does not begin to increase until 700 K, indicating that recombination is not active below this temperature. On the other hand, T_{on} for the 10 nm case is significantly lower (~ 250 K). Since the recombination is not active in this regime, the only means by which an increase in the DTA vs T curve can be realized is by annihilation of defects (interstitials and/or vacancies) at GBs. Since vacancies are immobile ($\delta = 5$) one can conclude that it is the diffusion and annihilation of interstitials that is responsible for $T_{on} \approx 250$ K. The fact that the interstitials are lost from the system is further evidenced by plotting the concentrations of interstitial at amorphization for the bulk and the 10 nm case in Fig. 6b. For bulk and the 10 nm case, at $\rho = 0.1$ the concentration of interstitials begin to decrease at ~ 250 K, which is the same as T_{on} . In the case of $\rho = 2$, the bulk shows a decrease in interstitial concentration at ~ 450 K, which is its T_{cr} , while in the 10 nm case, the interstitial concentration begins to decrease at ~ 250 K due to annihilation at the GB.

It is also instructive to examine the relative rates of production and annihilation of various defects. While vacancies and interstitials are being produced at equal rates ($\alpha = 0.5$), their annihilation rates are different. This imbalance between the rates of annihilation of vacancies and interstitials depends on both ρ and R . We first discuss the effect

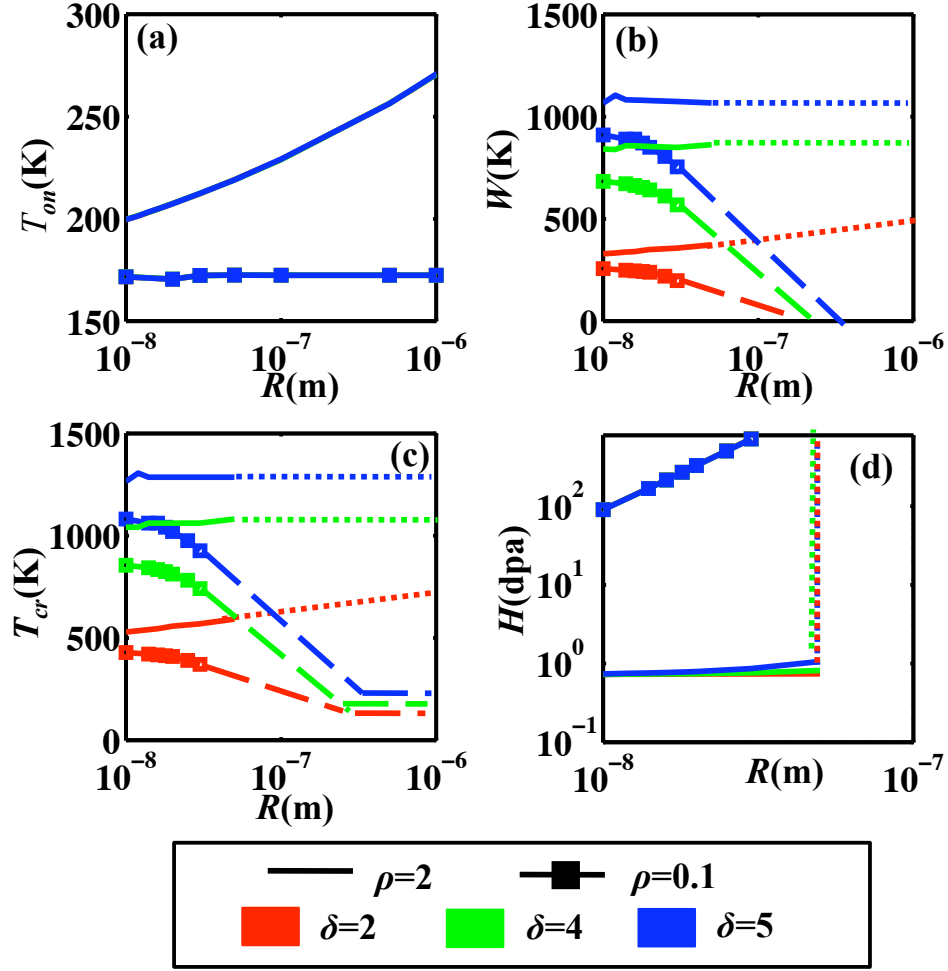


FIG. 5. Variation with respect to R of (a) Onset temperature T_{on} , (b) Step Width W , (c) Critical amorphization temperature T_{cr} and (d) Step height H . Bare lines represent $\rho = 2$ while lines with squares $\rho = 0.1$. The red, green and blue colors indicate $\delta = 2, 4$ and 5 , respectively. Long dashed and dotted lines indicate extrapolated values for the regions where the steps in the DTA vs T lied above a 1000 dpa for $\rho = 0.1$ and 2 , respectively

of grain size R on the imbalance of defect reactions, assuming a constant value of ρ . The larger the value of R , the greater the effective distances that interstitials have to travel and the more interstitials in the grains of the material are annealed by recombination with vacancies. Thus for a very large R ($R \sim \mu\text{m}$), the imbalance between interstitial and vacancy annihilation is small. For small R , interstitials can quickly diffuse and annihilate at the GB, even if the interstitials are near the grain center. Thus for small values of R ($\sim \text{nm}$), the imbalance between the annihilation of vacancies and interstitials is larger, with vacancies being annihilated at much lower rates than interstitials. This imbalance results in unrecombined vacancies being left behind in bulk and accumulation of these vacancies causes the material to amorphize. To understand the implication of this imbalance, we first recall that if the rates of recombination and annihilation at GBs occurred at the same rate, then the process of recombination would be more efficient in healing damage (decreasing defect concentration) than annihilation. It is because two defects are eliminated simultaneously during recombination of a Frenkel pair, in contrast to only one defect (usually the faster diffusing species) being eliminated by GB annihilation. Thus in case of very small R , the bulk of the grain is starved of interstitials due to which a significant number of vacancies is left behind in the bulk, causing amorphization. For a slightly larger R , recombination is more extensive, leaving behind a lower concentration of vacancies. Thus the concentration of vacancies left behind increases with decreasing R . Since T_{cr} is caused by vacancy motion, increasing R leads to a decrease in T_{cr} . This process by which the bulk of the grain is depleted of interstitials, leaving behind an excess of vacancies will be referred to as *interstitial starvation* (IS). The phenomenon of interstitial starvation is responsible for the observed decrease in T_{cr} with increase in R .

We note that IS resulted in the fine-grained material having higher T_{cr} than the coarse-grained material, only

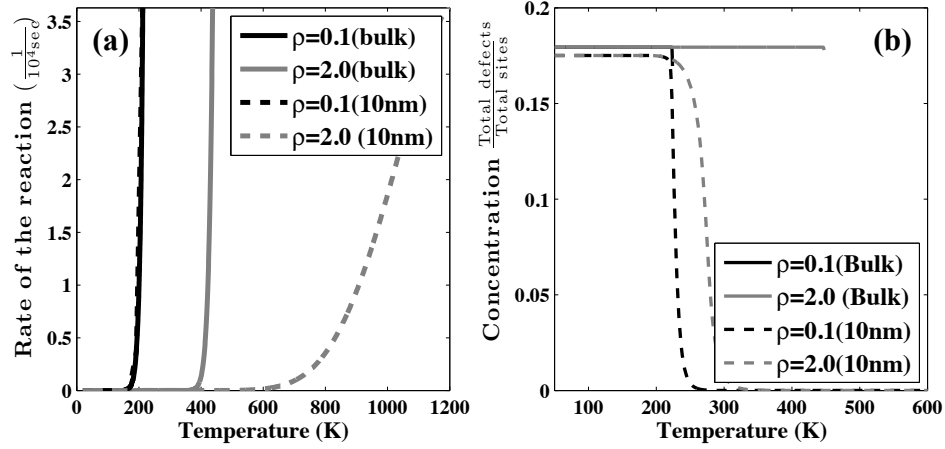


FIG. 6. (a) Rate of the recombination reaction for the generic material and (b) Concentration of the interstitials. Both the plots are made for the bulk and the 10 nm material for two values of ρ

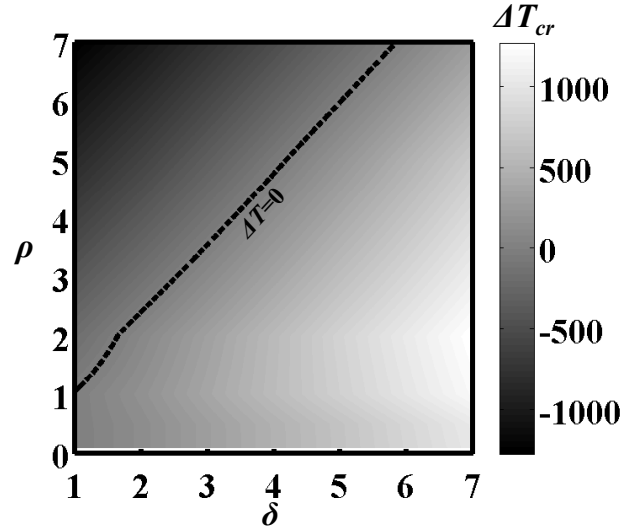


FIG. 7. The parameter ΔT_{cr} , which is the difference in the T_{cr} between the 10nm case and the ideal bulk case, for various values of ρ and δ . Positive values of ΔT_{cr} indicate that the 10 nm has a lower resistance to RIA when compared to the bulk material.

because, with the decrease in R , recombination occurred to a lesser extent and GB annihilation of interstitials increased. We can therefore define a regime of coupling between defect recombination kinetics and grain size effects. Specifically, decreasing the grain size will increase T_{cr} by the phenomenon of IS when the value of ρ is small enough so as to allow simultaneous recombination and GB annihilation in a given material. If ρ is large (> 2), recombination is suppressed irrespectively of the specific grain size. The only mechanism by which any defect can be eliminated from the system is by GB annihilation. Since GB annihilation is easier for small R , the T_{cr} will only increase with R for these large values of ρ as seen in Fig. 4c.

Since IS lowers radiation resistance of fine-grained material only for a certain range of ρ values, it is interesting to investigate how this range varies with δ . For this purpose we evaluate ΔT_{cr} , which is the difference in the T_{cr} between the 10 nm case and the ideal bulk material, for a range of δ and ρ . The results are shown in Fig. 7. Regions of positive ΔT_{cr} indicate values of ρ , δ , where the 10 nm material is more susceptible to RIA when compared to the ideal bulk, while regions of negative ΔT_{cr} correspond to the 10 nm materials having a better resistance. This kind of a map, which can be generated using a simple rate theory model for a desired grain size, can serve to make predictions which material may show an improved resistance to RIA due to grain refinement. Parameters needed to apply this model

to real materials are the kinetic barriers for defect diffusion and defect recombination.

4. Step height (H)

As shown in Fig. 4d, the step height H is independent of δ , but depends on ρ and R . Specifically, H increases with decreasing ρ in the range $0 \leq \rho \leq 2$, while H is constant for $\rho > 2$. Furthermore, H increases with R for a given ρ in the range $0 \leq \rho \leq 2$. To understand the physical origin of the variation of H with ρ we first need to understand the exact reason for the occurrence of the step in the DTA vs T curves. This step occurs approximately between T_0 (which is slightly greater than T_{on}) and the critical amorphization temperature T_{cr} (See Fig. 3). To explain why we see this region, we must analyze the behavior of solutions to Eq. 1 analytically. We first rewrite Eq. 1 for the vacancies (v) and interstitials (i) into the following form:

$$\frac{\partial c_v}{\partial t} = P_v - A_v, \quad (13)$$

$$\frac{\partial c_i}{\partial t} = P_i - A_i. \quad (14)$$

For each defect n , $A_n = A_n^{GB} + A_n^R$, where A_n^{GB} and A_n^R are the rates at which the defect n is annihilated by annihilation at GB and recombination, respectively. Both A_n^{GB} and A_n^R are positive. By subtracting Eq. 14 from Eq. 13 we get,

$$\frac{\partial c_v}{\partial t} - \frac{\partial c_i}{\partial t} = (P_v - A_v^{GB} - A_v^R) - (P_i - A_i^{GB} - A_i^R) = \Lambda. \quad (15)$$

In the above equation Λ is a measure of the imbalance in the rate of evolution of vacancies and interstitials. A positive Λ means that the rate of increase in vacancy concentration is greater than the rate of increase in interstitial concentration. Now, since the vacancies can be considered immobile nearly up to T_{cr} and since we are analyzing regions between T_0 (or T_{on}) and T_{cr} , we can assume that $A_v^{GB} \approx 0$ when $T_0 \leq T \leq T_{cr}$. In addition, since $P_v = P_i$ and $A_v^R = A_i^R = Kc_i c_v$, it follows that $\Lambda \approx A_i^{GB}$. A_i^{GB} can be looked upon as a volume averaged behavior of the term $\frac{D_i}{R^2} \frac{1}{r^2} \frac{\partial}{\partial r} (r^2 \frac{\partial c_n}{\partial r})$ (see Eq. 1) and it is given by $\frac{3D_i}{R^2} \int_0^1 \frac{\partial}{\partial r} (r^2 \frac{\partial c_n}{\partial r}) dr$. For a given set of boundary conditions, it can be seen that the quantity, $\int_0^1 \frac{\partial}{\partial r} (r^2 \frac{\partial c_n}{\partial r}) dr$ is non-dimensional and is a constant which we call Θ . Therefore, we can write, $A_i^{GB} = \frac{3D_i}{R^2} \Theta$. For an ideal bulk material $\Lambda = 0$ since $R = \infty$ and the only path to defect annihilation is a recombination of Frenkel pairs, which simultaneously eliminates vacancy and interstitial. Now we integrate Eq. 15 to obtain,

$$c_v - c_i \approx A_i^{GB} t = \frac{3D_i}{R^2} \Theta t > 0. \quad (16)$$

To determine if a positive Λ can cause c_i to decrease to very small values, which in turn results in vacancy driven amorphization, we examine the possibilities of c_i and c_v becoming zero during their evolution. Early on during the evolution (small t), both $\frac{\partial c_v}{\partial t}$ and $\frac{\partial c_i}{\partial t}$ are positive because the rate of production of defects (c and v) exceeds the rate at which they recombine or annihilate at the GB. Close to $t \approx 0$ the concentrations (c_i and c_v) and the gradients in the concentrations are small causing A_n^R and $A_n^{GB} \approx 0$. Thus, $\frac{\partial c_v}{\partial t}$ and $\frac{\partial c_i}{\partial t}$ are both equal to $P_v = P_i$ which is constant and positive. We note that if at some time $t = t_v$, $\frac{\partial c_v}{\partial t} = 0$, then Eq. 15 and Eq. 16 imply that $c_i < 0$, which is physically not permissible (concentrations are positive quantities). Therefore, the vacancy concentrations only increases with time. On the other hand, if at some time $t = t_i$, $\frac{\partial c_i}{\partial t} = 0$, then $c_v > 0$, which case is physically permissible. Thus, what we observe is that, for positive Λ , $\frac{\partial c_i}{\partial t}$ is initially positive and then becomes zero at a time $t = t_i$. For $t > t_i$, $\frac{\partial c_i}{\partial t} < 0$ and at a time $t_0 > t_i$, $c_i \approx 0$. If the material has not amorphized by t_0 , then for $t > t_0$ only the vacancies in the material drive amorphization. Thus for $t > t_0$, $c_v \approx A_i^{GB} t$ and using this expression for c_v in the criterion for amorphization (Eq. 11) we obtain $\Delta E_{am} \approx E_v A_i^{GB} t_{am}$, where t_{am} is the time at amorphization. We can rewrite $t_{am} \approx \frac{\Delta E_{am}}{E_v A_i^{GB}}$ and substitute it in the expression for the DTA

$$\text{DTA} = t_{am} \times \text{dose rate} \approx \frac{\Delta E_{am}}{E_v A_i^{GB}} \times \text{dose rate} \quad (17)$$

Now, when values of ρ are large enough for a given grain radius, R (e.g., $\rho \approx 2$), none of the interstitials that are produced are able to recombine with vacancies and the imbalance established by A_i^{GB} is large. From Eq. 17, a large value of A_i^{GB} means that the DTA is low. This trend can be seen in Fig. 2 in curves corresponding to $\rho \approx 2$ for the case when $R = 10$ nm. For very low values of ρ (≤ 1) nearly all of the interstitials recombine with vacancies and very

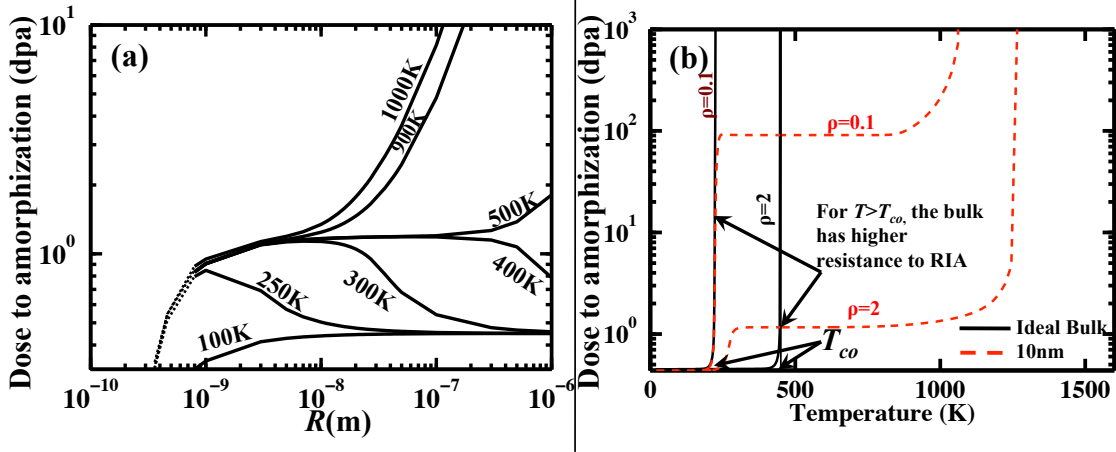


FIG. 8. (a) Variation of DTA with R at different temperatures ($\delta = 5, \rho = 2$), (b) DTA vs T curves for the 10 nm and ideal bulk material for $\delta = 5, \rho = 0.1, 2$, illustrating the temperature beyond which the ideal bulk has superior resistance to RIA. The crossover occurs at higher doses for low values of ρ

few interstitials are left near the GB to annihilate there. As a result the imbalance set by A_i^{GB} is small. Now, since $DTA \propto \frac{1}{A_i^{GB}}$, for small values of ρ the DTA is high. This trend of decreasing DTA with an increasing ρ for a given R can be seen in Fig. 2 for the 10 nm case and in Fig. 4d in the region $0 \leq \rho \leq 2$. Increasing ρ beyond 2 does not change A_i^{GB} significantly, since by $\rho = 2$ a stage has been reached when no interstitial recombines with the vacancy. Therefore, the step height H is independent of ρ for $\rho > 2$ as seen in Fig. 4d.

In the preceding discussion we gave reasons for why H varies with ρ , however further discussion is needed regarding the relative flatness of the DTA vs T curves for some values of ρ ($\rho > 2$ and $\rho = 0.1, 0.5$ and 1) and the relatively less pronounced steps as seen for $\rho = 1.2, 1.5$ in Fig. 2. For large values of ρ (such as $\rho \geq 2$) Frenkel pair recombination becomes impossible and all the interstitials have to be annihilated at the GB. Increasing T above T_0 , for such large ρ values does not change A_i^{GB} much. A constant A_i^{GB} implies a constant DTA (see Eq. 17), leading to a plateau between T_0 and T_{cr} , as seen in Fig. 2 for $\rho > 2$, $R = 10$ nm case. A_i^{GB} is also not sensitive to T for low values of ρ (e.g., $0.1, 0.5$, and 1), because the dominant mechanism of defect annihilation in this regime is Frenkel pair recombination. Consequently, the curves shown in Fig. 2 for this regime of ρ exhibit plateaus. In contrast, for intermediate values of ρ , A_i^{GB} becomes sensitive to T and the plateau between T_0 and T_{cr} is less pronounced (see curves for $\rho = 1.2, 1.5$ in Fig. 2 for the 10 nm case).

Finally, from Fig. 4d and Fig. 5d, we see that for $\rho = 0.1$, H increases with R . The increase of H with R can be explained in a manner similar to the variation of H with ρ , by considering the variation of A_i^{GB} with R (see Eq. 17). Specifically, we know that for a given ρ , A_i^{GB} is inversely proportional to R^2 . Therefore for a given ρ , as R increases, A_i^{GB} decreases, which means that DTA increases. Since H is a measure of DTA, this argument explains why an increase in R leads to an increase in H .

C. Is nanomaterial better? (Thermodynamic and kinetic considerations)

We now address the question of whether decreasing the grain size to the nanometer regime will improve resistance of a given material to RIA. As discussed in Section I, both an increased and a decreased resistance has been reported in literature, depending on the material itself and on the environment. To explain these trends, most authors used thermodynamic arguments. A decrease of nanomaterials resistance to RIA has been attributed to an increase in the free energy of the material due to the higher volume fraction of GBs, which energy drives the materials closer to the amorphization transition. In cases where nanomaterials have shown a superior resistance to radiation, it has been argued that a higher volume fraction of GBs provide a higher density of defect sinks and therefore lead to a more efficient damage recovery. Although these arguments are valid, they provide only a partial view of the processes that occur in nanomaterials and more specifically they do not take into account kinetic phenomena such as IS. The possibility of IS has been postulated to occur in nanomaterials by Shen *et. al.*⁵², but until the current study it has not been analyzed in a consistent framework for modeling amorphization.

To illustrate the contributions from thermodynamic and kinetic effects to RIA of nanomaterials, in Fig. 8a we analyze the DTA vs. R curve plotted for various temperatures. We choose $\delta = 5$ and $\rho = 2$ as an example. We plotted the curves for R values ranging from 0.8 nm to 1 μm . The curves for values of R lower than 0.8 nm were extrapolated from the general trend shown by these curves and is plotted using dashed line in Fig. 8a. For this case we find that for temperatures as low as 100 K, resistance of materials with small grain sizes (~ 10 nm) is negligible (very small DTA). This resistance increases with increasing R up to ~ 100 nm, beyond which size the DTA is constant with R . For intermediate temperatures (e.g., 250K, 300 K and 400 K), there is an optimum grain size $R = R_o$ for which the resistance to radiation is maximized. R_o increases with temperature and the grain-size dependence displays a crossover at a critical temperature T_{co} , which falls between 400 K and 500 K. This crossover is better illustrated in the Fig. 8b, where we plot the DTA vs. T curve for $R=10$ nm and the ideal bulk, for $\delta = 5$ and $\rho = 0.1, 2$. We can see that the 10 nm material has a superior resistance to RIA below T_{co} and inferior resistance above T_{co} , as compared to the bulk material. We note that the dose at crossover is lower for higher values of ρ , as shown in Fig. 8b. In Fig. 8a we see that beyond T_{co} , there is no longer a maximum in DTA vs R curve and the resistance to amorphization only increases with R . The occurrence of an optimum grain size R_o that maximizes resistance to RIA at a particular temperature below T_{co} has been reported previously in theoretical works⁶ and rate theory models³⁶. This phenomenon has been attributed to thermodynamic effects. Specifically, it has been pointed out that very small grain sizes have an inferior resistance as compared to polycrystalline samples because in this regime the amorphization is dominated by the effect of increasing GB energy with grain refinement. However, as we discuss below, the origin of the optimal grain size R_o is here dominated by kinetic configurations, and it is only for grain sizes in the order of 1nm or lesser where thermodynamic instability has any significant effect. Furthermore, interesting behavior is observed below T_{co} in the regime where the grain sizes are slightly increased but still below R_o . In this regime, contribution to energy from GBs is large enough to be the dominant factor in controlling the dependence of radiation induced amorphization on grain size. As R is increased in the regime ($R < R_o$), the contribution of energy from the GB is not high enough to cause amorphization and the resistance increases. At grain sizes above R_o , the resistance once again decreases with increasing R , since the annihilation of interstitials at GB becomes less effective in healing the damage due to increase in distances that defects need to diffuse before they reach GBs.

The temperature dependence of the optimum grain size (R_o) and of the crossover (shown in Fig. 8b for the 10 nm case) are the results of an increasing role of IS (discussed in section III B 3) with temperature. At a given R IS becomes more effective with increasing T , leaving behind more vacancies which then can contribute to the energy increase. Furthermore, we have seen from section III B 3 that IS is more effective in smaller grains, since the interstitials can annihilate at the GBs at a higher rate than they can do so in a larger grains where recombination processes in grain interior still dominates and effectively heals radiation damage. An increased concentration of vacancies left behind in materials with smaller grains due to IS combined with the increased rate rate of IS with T , results in the R_o increasing with T . Below T_{co} the rate of GB annihilation is still slow enough to allow some interstitials in the bulk to recombine with vacancies. When $T > T_{co}$, no interstitial is actually left behind (all of them annihilate at the GB) and vacancies build up causing amorphization. Alternatively, one may say that for $T > T_{co}$, recombination will be present only in the limit of an infinite R , which is the ideal bulk case, meaning that the $R_o \rightarrow \infty$, since the interstitials cannot annihilate at the GB. The main impact of the kinetic effects, such as IS, is that, the answer to the question of how grain refinement affects resistance to RIA depends on irradiation temperature. For $T < T_{co}$ and $R > R_o$, increasing R decreases the resistance of materials to RIA. When, $R < R_o$ or $T > T_{co}$ increasing R decreases the resistance to RIA.

D. Silicon carbide (Variation of T_{cr} with R)

Silicon carbide (SiC) is a promising candidate for use as a structural and cladding material in next generation fusion and fission reactors^{37,54,55}. RIA is an important issue for this material, especially at temperatures below 500 K. Specifically, experiments on single crystal SiC reported T_{cr} of 340 K for electron irradiation³⁸, 420 K for irradiation with Si^+ ions⁵¹, and 500 K for irradiation with Xe ions⁵³. Grain refinement to the nanometer regime is one option that is being considered for overcoming the sensitivity of the bulk material to RIA. Consequently, radiation resistance of nanocrystalline SiC has been a subject of a number of experimental^{56,57} and modeling^{21,23,58} studies. For example, Jamison *et. al.*⁵⁸ conducted 1MeV Kr^+ radiation on SiC with 10 nm and 45-55 nm grain diameter and reported corresponding DTA vs T curves. The maximum experimental dose used in these experiments was 3 dpa and it was found that at temperatures below 400 K, 10 nm samples required a lower dose to amorphize when compared to 45-55 nm samples. Using a simple logarithmic fit to the DTA vs T data, the authors predicted T_{cr} for the 10 nm materials to be 610 K while T_{cr} for the 45-55m case was 485 K. The larger T_{cr} for smaller grain size samples suggests that in nanocrystalline SiC may be more susceptible to radiation damage than its polycrystalline counterpart.

Using the rate theory framework described in section IIB 2, we investigate RIA in SiC. Formation and migration

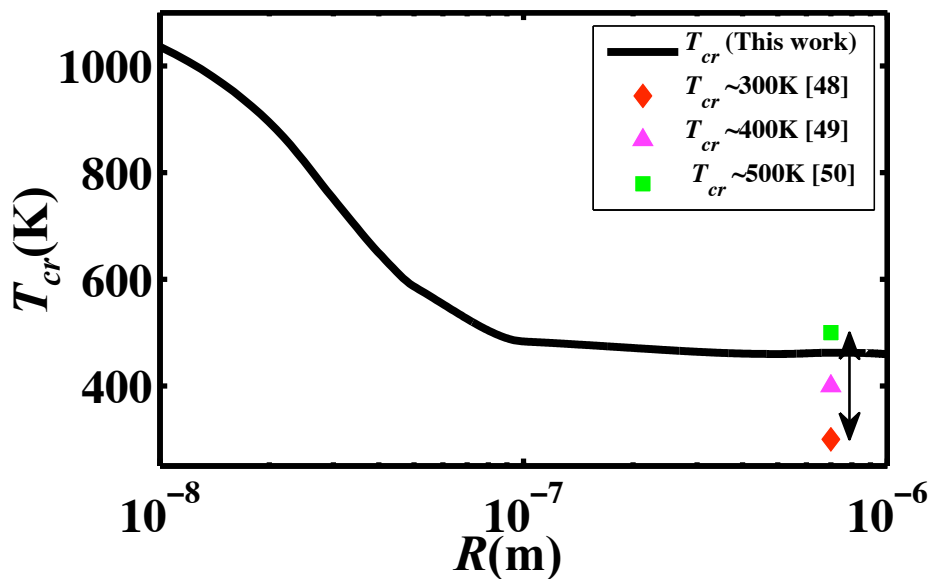


FIG. 9. Variation of T_{cr} with R for SiC using an *ab-initio* informed rate theory model. The symbols indicate the experimental T_{cr} values^{38,51,53}. The double arrow shows the range for T_{cr} obtained from experiments.

energies of defects as well as defect reaction energies used in our study are reported in Tables II and III. This set of *ab initio* energies constitutes a complete and a highly accurate database for energetics of point defects in SiC and therefore it is reasonable to expect that our rate theory model captures the correct physics in the regime where point defects dominate radiation response of SiC. We find that phenomenon analogous to IS observed in a single-component material X (see Section. III B), takes place also in SiC. Specifically, reaction R.6₁ (see Table III) was found to leave unrecombined vacancies in the grains. The low barrier (0.69 eV) of this reaction results in C_i forming a bound complex with Si_C , which decreases the concentration of free interstitials. The energy to dissolve this complex is 1.75 eV⁴⁵ and therefore C interstitials are trapped and prevented from recombination with C vacancies. This easy trapping of interstitials by Si_C combined with the fact that the bound complex has a formation energy lower by ~ 1.2 eV when compared to the cumulative formation energy of the constituent defects (C_i and Si_C), results in a formation of a small step in the DTA vs T for ideal bulk SiC. After this step, we observe a plateau in the DTA vs T plot and we find that amorphization in the plateau regime is dominated by accumulation of vacancies and not of the C_i - Si_C complex. For finite grain sizes, in addition to the loss of free interstitials through R.6₁, interstitials are also lost to the GB due to relatively low barrier for C_i migration (0.67 eV cf. Table. II), which in turn leads to the IS effect. This loss of interstitials to the GB is enhanced even further by the high recombination barrier for R.1, which is 0.92 eV. Due to this high barrier for R.1, the interstitials choose to either form the complex with Si_C or diffuse to the GB. Since the loss of free interstitials by diffusion to the GB (IS) is higher in smaller grains than in larger ones, we found that T_{cr} was higher for smaller grains.

While our model demonstrates that IS is likely to be present in materials such as SiC, we do not expect the predictions of DTA values made by our model for SiC to be quantitative. This limitation is due to the importance of clustering, which can dramatically change defect thermodynamics and kinetics, and therefore DTA. It has been hypothesized that at higher defect concentrations, defects in SiC can cluster^{46,59} and clustering is not included in our model. The radiation response property that is expected to be captured quantitatively by our model, even if defect clustering takes place during irradiation, is the critical amorphization temperature T_{cr} . The ability of the model to capture T_{cr} is derived from the fact that T_{cr} is controlled by kinetic barriers of defect reactions at low defect concentrations, which are correctly reproduced in our model, and not by formation energies of defects³⁵ at high concentrations (which control DTA in our model). Here, we assume that any defect reactions that involve clusters (e.g., cooperative rearrangement of many atoms) do not cause any significant recovery of radiation damage in SiC. In materials where such cooperative rearrangement of atoms heal significant damage a point defect model of the kind presented in this paper would overestimate T_{cr} . In addition to trapping effects, the presence of clusters could change defect evolution properties in multiple ways, including total and relative vacancy and interstitial concentrations, enhanced recombination through strain effects and altered recombination pathways, altered transport properties through cluster mobility, and altered production rates through cascades overlapping with existing damage clusters.

The potential impact of clusters through these and related effects are beyond the scope of the present study and will require further work.

In light of this discussion, our investigation of grain size effects on RIA resistance in SiC are focused on T_{cr} and its variation with R (see Fig. 9). Furthermore, since the maximum doses used in irradiation experiments of SiC is about 20 – 30 dpa²⁹, we do not analyze doses up to as high as 1000 dpa (as we did for the generic material). We take T_{cr} to be the temperature corresponding to 30 dpa so that we can perform comparison between our data and experiments. Based on the curves in Fig. 9 we conclude that fine-grained SiC has an inferior resistance to RIA when compared to the coarse-grained SiC, consistently with what has been reported in recent experiments⁵⁸. In our model, the 10 nm sample has T_{cr} approximately equal to 1050 K, while the bulk (single crystal) SiC has a T_{cr} of about 450 K. As shown in Fig. 9, T_{cr} predicted by our model for a single crystal SiC falls into the range for experimental measurements. Our prediction of T_{cr} for 10 nm grain size differs from the value of 700K reported by Jamison *et al*⁵⁸. However, one needs to keep in mind that T_{cr} in Ref.⁵⁸ was predicted by fitting experimental data measured at lower temperatures to a relatively simple one-parameter amorphization model and therefore there might be some uncertainty in the exact value of T_{cr} . Based on the discussion in the previous paragraph, we can attribute the deterioration of radiation resistance with grain refinement to the starvation of C_i . C_i have a lower barrier for diffusion to GBs than they have to recombine with V_C . As a result, a significant fraction of C_i migrates to GBs, leaving behind an excess of V_C , which defects in turn amorphize the material. It is instructive to ask whether it is possible that the inferior resistance of fine grains to RIA is due to thermodynamic effects (i.e., an increase in free energy of fine-grained materials due to the larger volume fraction of GBs), rather than from IS. This GB-related thermodynamic effect can be ruled out as the only factor driving radiation-induced amorphization by noting that the contribution from GB energy to the total energy in the material with grains as small as $R = 10$ nm is only about 2.8% of the E_{am} value and therefore this contribution cannot account for a significant contribution to the onset of amorphization.

We note that the predicted T_{cr} becomes quite extreme at low grain size, reaching over 1000K for a 10nm particle size. This behavior in the model requires that the grain boundaries can absorb all the interstitials to allow IS to occur. While this is possible, other processes, such as grain boundary saturation, growth of the grain boundaries from the absorbed interstitials, C precipitation, or interstitial emission [20] might occur, changing the predicted T_{cr} . These effects are not included in our model. Further studies on the exact mechanisms for accommodating large excesses of C_i at grain boundaries in SiC will be needed to assess if the simple perfect sink approximation breaks down under some conditions and what consequences this breakdown might have for amorphization.

Finally, it is worth discussing which defect energetics are responsible for the value of T_{cr} observed in experiments and predicted by our model. It has been sometimes conjectured that T_{cr} is correlated with migration energy of a slower interstitial in SiC. To show the effect of migration barriers on T_{cr} we perform rate theory simulations of electron irradiation in SiC in the case where there are no recombination or trapping barriers present (the so-called no-barrier model as discussed in Ref.³⁵). In this case we found T_{cr} to be equal to ~ 220 K and set by Si_i mobility (leading to annihilation of Si_i with V_{Si}), which is higher than C_i mobility (see Table II). This value of T_{cr} is lower by ~ 100 K than the lower limit of the experimentally measured values of T_{cr} , which is between 340K³⁸ to 420K^{51,53}. This analysis shows that energy barriers to migration of point defects in SiC are too low to account for experimentally measured critical amorphization temperatures. On the other hand, when all the barriers to defect reactions (as determined in Ref.⁴⁵) are included in the simulations, the amorphization temperature predicted by the model is 450 K, which is within the range of experimentally predicted values and in particular it is close to $T_{cr} \sim 420$ K measured in more recent experiments^{51,53}. We find that this T_{cr} is not controlled by migration barriers of defects, but by the second step in the kick-out reaction (R6.2 in Table III). In this step C_i kicks out a Si antisite (Si_C), leading to formation of a Si interstitial (Si_i). The Si_i then can readily recombine with the V_{Si} , which leads to healing of the Si defects. The barrier to the kick-out reaction is 1.35 eV and it is responsible for the predicted amorphization temperature of 450 K. Based on our model we propose that the physical origin of amorphization temperature in SiC should be reinterpreted.

IV. CONCLUSION

Rate theory was used to predict the dose to amorphization (DTA) vs T curves of a generic one component material as a function of its grain size. The curves for the ideal bulk (single crystal) material showed a temperature at which the DTA increases exponentially while the curves for the nanomaterial had several other features. The fine-grained material showed an onset temperature T_{on} (where DTA increases by a finite amount), a step with a definite width (W) and height (H), and a final increase in the DTA, which defined the critical temperature T_{cr} . All these features were studied as a function of the grain radius R , a vacancy migration barrier δ , and a Frenkel pair recombination barrier ρ (where δ and ρ are given in units of the interstitial migration energy). Among other trends, we found that T_{cr} can either increase or decrease with R , depending on the values of R , as well as of ρ and δ . We discovered that in addition to thermodynamic arguments made previously in literature, an important effect in radiation resistance of

nanomaterials is the kinetic effect of interstitial starvation. In this phenomenon, a significant number of interstitials diffuse and are annihilated at GBs, leaving behind unrecombined vacancies in the bulk of the material. Accumulation of these vacancies drives RIA. Furthermore, we found that IS is more pronounced (i.e., occurs at lower doses) when the barrier ρ was greater than unity, which means that the barrier for interstitial-vacancy recombination is higher than that for interstitial diffusion. Such situation results in the interstitial diffusing to the GB and leaving behind many unrecombined vacancies, which in turn increases the systems energy and causes amorphization.

To identify regimes of R and T where grain refinement leads to enhancement or deterioration of radiation resistance as compared to the bulk material, we plotted the DTA vs R for several T . We considered two cases one where the recombination barrier of Frenkel pair is high and one where it is comparable to the interstitial migration barrier. For high recombination barrier (inspired by the SiC case), we found that there exists a crossover temperature T_{co} , where the grain refinement changes from beneficial to detrimental at doses which are low enough to be conceived in experiments. Furthermore, there is also a temperature dependent optimum grain radius R_o for which radiation resistance is maximized. Both T_{co} and R_o depend on the kinetic parameters represented by ρ and δ . In general, it was found that below T_{co} and for values of $R < R_o$, the resistance to RIA always increases with R which means that smaller grains have lower resistance to RIA. In the same temperature regime, but above R_o , the resistance decreases with increasing R , indicating that finer grains have better radiation resistance. Above T_{co} , the fine-grained material always has a lower resistance to RIA when compared to the coarse grained material. In comparing a low recombination barrier to a higher one, we found that the crossover temperature might be lower, but the dose at which the crossover occurs is much higher.

Thus in addition to the effects of grain refinement the effects of temperature were shown to play an important role in affecting radiation damage of a material. Chimi *et. al.*⁸ also studied experimentally the effect of temperature on radiation resistance. They found that, at low temperature nanocrystalline Au was worse than the bulk material. At higher temperatures they found that the nano crystalline material was better than the bulk material. The reason for the high temperature improvement in radiation resistance was concluded to be the diffusion and annihilation of point defects at the grain boundaries. The low temperature inferiority in radiation resistance was hypothesized to be due to enhanced defect production at grain boundaries, short collision sequence and trapping of defects. In our current model, we have not included these effects. Further, atomistic level calculations might shed light on these aspects.

In summary, we have shown that, whether refinement of grain size to the nanometer regime will improve radiation resistance could depend on the values of the kinetic parameters (migration and recombination barriers) and the temperature for the intended use of the material. The phenomenon of interstitial starvation could render the nano crystalline material more susceptible to radiation damage than the coarse grained counterpart. One should keep in mind that there are other processes which could affect the results of this conclusion. For example, in-cascade amorphization could take place instead of the the energy based method used in this paper. Defect clusters may form and affect processes such as the defect production rate, recombinations and diffusion of simple defects. The defect clusters may themselves diffuse and change the resistance to radiation damage in complicated ways. Including these effects in the model could explain some of the discrepancies with some experimental work like that of Chimi *et. al.*⁸. Multicomponent oxides like $MgGa_2O_4$ ⁶ could have complicated kinetic phenomenon taking place which our simple model does not capture. Detailed understanding of the operating defects, defect clusters is needed to explain the exact behavior of such oxides. Nevertheless our results demonstrate that recombination barrier is a critical parameter to include in a model and in a number of materials (such as SiC) which can lead to interstitial starvation

When applied to the case of SiC, our rate theory model predicts that critical amorphization temperature of nanocrystalline SiC is higher than of its polycrystalline counterpart. This trend is consistent with recent experiments on the same materials^{57,58}. The presence of a high kinetic barrier for the recombination of C_i with V_C leads to increase in interstitial starvation, which in turn leaves excess vacancies in the interior regions of the grain and contributes to amorphization. Interstitial starvation is more pronounced for materials with smaller grain sizes and that explains why grain refinement in SiC leads to deterioration of resistance to RIA. We also found that the energy barrier that controls the critical amorphization temperature (T_{cr}) corresponds to the kicking out of Si_C by C_i , for which the barrier is 1.35 eV.

V. ACKNOWLEDGEMENT

We are thankful to the US Department of Energy, Office of Basic Energy Sciences for supporting this project through grant DE-FG02-08ER46493.

-
- * n.swaminathan@iitm.ac.in
† ddmorgan@wisc.edu
‡ szlufarska@wisc.edu
- ¹ A. T. Motta, *J. Nucl. Mater.* **244**, 227 (1997).
 - ² V. I. Ivashchenko, P. E. A. Turchi, and V. I. Shevchenko, *Phys. Rev. B* **75**, 085209 (2007).
 - ³ M. Ishimaru, I.-T. Bae, A. Hirata, Y. Hirotsu, J. A. Valdez, and K. E. Sickafus, *Phys. Rev. B* **72**, 024116 (2005).
 - ⁴ M. L. Swanson, J. R. Parsons, and C. W. Hoelke (Gordon and Breach, Newyork, 1971) pp. 359–359.
 - ⁵ J. Zhang, J. Lian, S. Fuentes, Antonio, F. Zhang, M. Lang, F. Lu, and C. Ewing, *Appl. Phys. Lett* **94**, 243110 (2009).
 - ⁶ T. D. Shen, *Nucl. Instrum. Meth. B.* **266**, 921 (2008).
 - ⁷ M. Rose, G. Balogh, A, and H. Hahn, *Nucl. Instrum. Methods Phys. Res., Sect B* **127/128**, 119 (1997).
 - ⁸ Y. Chimi, A. Iwase, N. Ishikawa, M. Kobiyama, T. Inami, and S. Okuda, *J. Nucl. Mater.* **297**, 355 (2001).
 - ⁹ H. Wang, R. Araujo, J. G. Swadener, Y. Q. Wang, X. Zhang, E. G. Fu, and T. Cagin, *Nucl. Instrum. Methods Phys. Res., Sect B* **261**, 1162 (2007).
 - ¹⁰ A. Meldrum, L. Boatner, A, and R. Ewing, *C, Phys. Rev. Lett.* **88**, 025503 (2001).
 - ¹¹ A. Meldrum, L. Boatner, A, and C. Ewing, *Rodney, Nucl. Instrum. Methods Phys. Res., Sect B* **207**, 28 (2003).
 - ¹² K. E. Sickafus, H. Matzke, K. Yasuda, P. Chodak, R. A. Verall, P. G. Lucuta, H. R. Andrews, A. Tuross, N. Fromknecht, and N. Baker, *Nucl. Instrum. Methods Phys. Res., Sect B* **141**, 358 (1998).
 - ¹³ B. Johannessen, P. Kluth, D. Llewellyn, G. J. Foran, D. J. Cookson, and M. C. Ridgway, *Appl. Phys. Lett.* **907**, 073119 (2007).
 - ¹⁴ M. Samaras, P. M. Derlet, H. Van Swygenhoven, and M. Victoria, *Phys. Rev. Lett.* **88**, 125505 (2002).
 - ¹⁵ M. Samaras, P. M. Derlet, H. Van Swygenhoven, and M. Victoria, *Philos. Mag* **83**, 3599 (2003), sp. Iss. SI.
 - ¹⁶ M. Samaras, P. M. Derlet, H. Van Swygenhoven, and M. Victoria, *J. Nucl. Mater* **351**, 47 (2006).
 - ¹⁷ R. E. Stoller, P. J. Kamenski, and Y. N. Osetsky, in *Mater. Res. Soc. Symp. Proc. Vol. 1125* (2009) pp. 1–12, r05-05.
 - ¹⁸ P. C. Millett, D. S. Aidhy, T. Desai, S. R. Phillipot, and D. Wolf, *Int. J. Mater. Res.* **100**, 550 (2009).
 - ¹⁹ P. C. Millett, D. Wolf, T. Desai, and V. Yamakov, *Appl. Phys. Lett* **93**, 161902 (2008).
 - ²⁰ X.-M. Bai, A. F. Voter, R. G. Hoagland, M. Nastasi, and B. P. Uberuaga, *Science* **327**, 1631 (2010).
 - ²¹ N. Swaminathan, P. J. Kamenski, D. Morgan, and I. Szlufarska, *Acta. Mat.* **58**, 2843 (2010).
 - ²² A. Moriani and F. Cleri, *Phys. Rev. B* **73**, 214113 (2006).
 - ²³ F. Gao, D. Chen, W. Hu, and W. J. Weber, *Phys. Rev. B* **81**, 184101 (2010).
 - ²⁴ L. Van Brutzel and E. Vincent-Aublant, *J. Nucl. Mater.* **377**, 522 (2008).
 - ²⁵ L. Van Brutzel, E. Vincent-Aublant, and J. M. Delaye, *Nucl. Instrum. Meth. B.* **267**, 3013 (2009).
 - ²⁶ E. Vincent-Aublant, J. M. Delaye, and L. Van Brutzel, *J. Nucl. Mater.* **392**, 114 (2009).
 - ²⁷ X.-M. Bai and B. P. Uberuaga, *Philos. Mag.* , 1 (2012).
 - ²⁸ G. S. Was, *Fundamentals of radiation material science*, 1st ed. (Springer, New York, 2007) Chap. 5.
 - ²⁹ J. Zinkle, S and L. L. Snead, *Nucl. Instrum. Methods Phys. Res., Sect B* **116**, 92 (1996).
 - ³⁰ H. Mori and H. Fujita, *Jpn. J. Appl. Phys.* **21**, L494 (1982).
 - ³¹ W. L. Gong, L. M. Wang, R. C. Ewing, and J. Zhang, *Phys. Rev. B* **54**, 3800 (1996).
 - ³² D. F. Pedraza, *J. Mater. Res.* **1**, 425 (1986).
 - ³³ A. T. Motta, *J. Nucl. Mater.* **270**, 174 (1999).
 - ³⁴ A. T. Motta and D. R. Olander, *Acta Metall. Mater.* **38**, 2175 (1990).
 - ³⁵ N. Swaminathan, D. Morgan, and I. Szlufarska, *J. Nucl. Mater.* **414**, 431 (2011).
 - ³⁶ I. A. Ovid'ko and A. G. Sheinerman, *Appl. Phys. A-Mater* **81**, 1083 (2005).
 - ³⁷ "A technology roadmap for generation iv nuclear energy systems, gif-00200," (2002).
 - ³⁸ H. Inui, H. Mori, A. Suzuki, and H. Fujita, *Phil. Mag. B.* **65**, 1 (1992).
 - ³⁹ T. R. Waite, *J. Chem. Phys.* **28**, 103 (1958).
 - ⁴⁰ G. Roma and J.-P. Crocombette, *J. Nucl. Mater.* **403**, 32 (2010).
 - ⁴¹ G. Gilmer, T. D. de la Rubia, D. Stock, and M. Jaraiz, *Nucl. Instrum. Methods Phys. Res., Sect B* **102**, 247 (1995).
 - ⁴² F. Gao, W. J. Weber, M. Posselt, and V. Belko, *Phys. Rev. B* **69**, 245205 (2004).
 - ⁴³ D. Shrader, S. M. Khalil, J. Heim, A. I. Szlufarska, and D. Morgan, *J. Nucl. Mater* **31**, 257 (2011).
 - ⁴⁴ M. Wojdyr, S. Khalil, Y. Liu, and I. Szlufarska, *Model. Simul. Mater. Sc.* **18**, 075009 (2010).
 - ⁴⁵ M. J. Zheng, N. Swaminathan, I. Szlufarska, and D. D. Morgan, To be submitted , 1 (2011).
 - ⁴⁶ M. Bockstedte, A. Mattausch, and O. Pankratov, *Phys. Rev. B* **69**, 235202 (2004).
 - ⁴⁷ G. Lucas and L. Pizzagalli, *J. Phys.: Condens. Matter* **19**, 086208 (2007).
 - ⁴⁸ M. Koiwa and S. Ishioka, *Phil. Mag. A.* **47**, 927 (1983).
 - ⁴⁹ A. R. Allnatt and A. B. Lidiard, *Atomic transport in solids*, 1st ed. (Cambridge University Press, Cambridge, 1993).
 - ⁵⁰ J. Tucker, R. Najafabadi, T. Allen, and D. Morgan, *J. Nucl. Mater.* **405**, 216 (2010).
 - ⁵¹ L. Snead, L. J. Zinkle, S, C. Hay, J, and C. Osborne, M, *Nucl. Instrum. Methods Phys. Res., Sect B* **141**, 123 (1998).
 - ⁵² D. Shen, Tong, S. Feng, M. Tang, and A. Valdez, James, *Appl. Phys. Lett* **90**, 263115 (2007).
 - ⁵³ W. J. Weber, N. Yu, and L. M. Wang, *J. Nucl. Mater.* **253**, 53 (1998).
 - ⁵⁴ T. R. Allen and D. C. Crawford, *Proceedings of ICAPP '03, Cordboa, Spain, American Nuclear Society* , 3237 (2003).

- ⁵⁵ S. Zinkle and J. Busby, *Mater. Today*, 12 (2009).
- ⁵⁶ W. Jiang, H. Wang, I. Kim, T. Bae, I. G. Li, P. Nachimuthu, Y. Zhang, and J. Weber, *Phys. Rev. B*, 161301 (2009).
- ⁵⁷ W. Jiang, H. Wang, I. Kim, Y. Zhang, and W. J. Weber, *J. Mater. Res.* **25**, 2341 (2010).
- ⁵⁸ L. Jamison, P. Xu, K. Sridharan, and T. Allen, "Radiation resistance of nanocrystalline silicon carbide," in *Advances in Materials Science for Environmental and Nuclear Technology II* (John Wiley & Sons, Inc., 2011) pp. 161–168.
- ⁵⁹ Z. Rong, F. Gao, W. J. Weber, and G. Hobler, *J. Appl. Phys.* **102**, 103508 (2007).